Influence of plasticity on inertialess viscoelastic instabilities in elongational flow regimes

V. Dzanic ◉,[1] C. S. From ◉,[2] and E. Sauret ◉[1,*]

[1]*School of Mechanical, Medical, and Process Engineering, Faculty of Engineering,*
Queensland University of Technology, QLD 4001, Australia
[2]*Department of Chemical Engineering, University of Manchester, Manchester M13 9PL, United Kingdom*

Many important practical applications involving porous media, cosmetics, biological systems, and food processing involve the transport of non-Newtonian fluids, which possess nonlinear material properties. Elastoviscoplastic fluids are indeed a complex example, simultaneously involving viscous, elastic, and plastic properties. In this study, we conduct numerical simulations of elastoviscoplastic fluids using a hybrid lattice Boltzmann solver in order to investigate the impact of plasticity, characterized by the Bingham number, on inertialess viscoelastic instabilities at high Weissenberg numbers. Results obtained using the four-roll mill and cellular-forcing scheme benchmark cases, which produce a strong elongational flow regime, reveal the emergence of three distinct flow states over time, namely a gradual shift from a laminar steady state to periodic orbits and ultimately evolving into aperiodic flow fluctuations during the late stages. The transition and behavior between these different flow states are found to strongly depend on the interplay between elasticity and plasticity. We demonstrate that the general effect of the Bingham number is to increase the unyielded regions in the fluid, which although appears initially contained in the vortical regions, naturally emerges in the vicinity of the polymer birefringent strands over time. The eventual effect is to laminarize and suppress the flow fluctuations of the viscoelastic instability in the late stages. Ultimately, this work demonstrates the impact of plasticity on the already complex inertialess viscoelastic instabilities that develop in the presence of strong elongational flow regimes, wherein the results provide an avenue for controlling the instability mechanism.

I. INTRODUCTION

Fluids characterized by nonlinear material properties, so-called non-Newtonian fluids, are ubiquitous in everyday life. They exhibit complex structural and deformation effects, making their behavior more intricate compared to their Newtonian counterparts. These additional nonlinear effects often include a shear-dependent viscosity, yield stress, and stress relaxation. Some of these effects are readily encountered in viscoelastic fluids, which involve mixing polymer additives with a solvent, giving rise to interesting time-dependent flow dynamics not experienced in purely Newtonian flows [1–4]. It is well known that the addition of these polymer molecules generate an anisotropic elastic stress contribution that transitions the flow to a chaotic regime, coined elastic turbulence (ET) [1,2]. This complex phenomenon is commonly characterized by enhanced mixing [2–5], increased flow resistance [2–4,6,7], as well as strong flow fluctuations, characterized by a broadband spectrum [1–4,8]. Remarkably, the nonlinearity of this viscoelastic instability is sourced

---

*emilie.sauret@qut.edu.au

063301-1

from purely elastic effects, characterized by high Weissenberg numbers (Wi $= \lambda \dot{\gamma} \gg 1$), whereby polymers are advected faster than their characteristic relaxation time λ in the presence of high shear rates $\dot{\gamma}$. This, in turn, allows for a transition into instability even with vanishingly small Reynolds numbers (Re $\ll 1$) [1–4]. This unique feature clearly allows the ability to provide enhanced mixing and fluid displacement capabilities in otherwise challenging conditions, thus allowing for viscoelastic instabilities to receive tremendous attention from various fields involving porous media [7,9–17] and microfluidic applications [18–21].

In addition to an elastic response, several other non-Newtonian features are often present in viscoelastic fluids and can coexist simultaneously. One such example involves the combination of viscous, elastic, and plastic properties, the so-called elastoviscoplastic (EVP) fluids. Specifically, these types of fluids transition between solidity and fluidity depending on the magnitude of the applied stress. Below a critical threshold termed the "yield stress," which is defined through the Bingham number (Bi), these materials demonstrate solidlike behavior, while exceeding this threshold causes them to flow like a liquid [22–24]. Such complex flow behavior is readily encountered in everyday fluids, such as toothpaste, cosmetics, and mud [23], as well as various practical flow applications involving mining [25,26], sewage treatment [27], and paper fabrication [28], to name a few.

Notably, EVP fluids experience elasticity in both their solid as well as liquid states, thus providing an avenue to transition into strong elastic flow behavior. However, despite the numerous studies performed to analyze these elastic effects in viscoelastic flows [3,4,29], much less attention has been given to EVP fluids. This can be partly attributed to the numerical complexity associated with simultaneously modeling the nonlinear material properties of EVP fluids. Unlike the well-established and continual advancements in the numerical viscoelastic research community [30], only recently have numerical studies emerged for EVP fluids [31–37]. This is largely attributed to the seminal work by Saramito *et al.* [24] who proposed a constitutive model (hereinafter, referred to as the Saramito model) for EVP fluid flows based on fundamental thermodynamic principles. Specifically, the Saramito model reproduces a viscoelastic solid, predicting only recoverable Kelvin–Voigt viscoelastic deformation for stresses lower than the yield stress, whereas the model describes a viscoelastic Oldroyd-B fluid for stresses higher than the yield stress. The combined properties of elasticity and plasticity have allowed the model to accurately capture experimental observations of EVP fluids. Specifically, studies by Cheddadi *et al.* [38] and Fraggedakis, Dimakopoulos, and Tsamopoulos [33] involved simulating the creeping flow behavior (Re $\ll 1$) of EVP fluids around a circular obstacle under low elasticity [Wi $\sim \mathcal{O}(0.1 - 1)$] using the Saramito model and were able to predict the experimentally observed fore–aft asymmetry and also the negative wake region after the obstacle [39,40]. Further studies have involved applying the Saramito model to investigate the flow of EVP fluids through porous media [35,36,41,42]. In their work, De Vita *et al.* [35] found that for a symmetrical porous constriction array, the yielded areas coincided with the shear-dominant regions of the flow, whereas the EVP fluid remained unyielded in locations of mixed flow (i.e., elongation and shear). The role of elasticity was subsequently investigated by Chapmarian *et al.* [42] for the same pore geometry by comparing viscoplastic and EVP fluids. The authors demonstrate that even low elastic effects [Wi $\sim \mathcal{O}(10^{-2})$] are capable of increasing the dynamic unyielded surfaces when compared to the viscoplastic solution. This physical discrepancy is attributed to the elastic nature of the unyielded regions in the EVP fluid, which can indeed possess a nonzero strain rate [38,42]. Moreover, a recent study by Varchanis *et al.* [43] involved experimentally and numerically investigating EVP fluids under steady, planar elongation, wherein the normal stresses that developed due to the elastic stress contribution caused a significant deviation of the ratio of the elongational to the shear yield stress from the standard value predicted by ideal viscoplastic theory, thus further demonstrating the complex and nontrivial behavior of EVP fluids.

In the context of observing the role of plasticity in EVP fluids with large elasticity [Wi $\sim \mathcal{O}(10^1)$], Parvar *et al.* [36] recently demonstrated for two-dimensional (2D) randomized porous media that elastic stresses help in overcoming the yield criteria. These large elastic effects at Re $= 1$ were shown to increase with both Wi and Bi, providing an avenue to eventually transition the EVP

flow into unsteady turbulent-like flow behavior. However, the general behavior and characterization of the inertialess turbulent EVP flow regime was beyond the scope of the investigation and thus remained unaddressed. Much of the existing attention has instead focused on characterizing the role of plasticity in inertial turbulent flows of EVP fluids [31,32,34], whereby the studies by Rosti *et al.* [32] and Le Clainche *et al.* [34] involved studying turbulent channel flow of an EVP fluid at Re = 2048 and Wi = 0.01 with varying Bi numbers. Both studies demonstrate that for low Bi values (Bi <1), the EVP flow retains most of the Newtonian turbulent flow features. However, increasing the plasticity to intermediate Bi values (Bi∼1) is accompanied by enhanced flow fluctuations and intermittency, resulting from the dynamic yielding and unyielding process in the center of the channel. The enhanced intermittency with Bi has also been recently observed by Abdelgawad, Cannon, and Rosti [31] for homogeneous isotropic turbulent flow of EVP fluids at Wi ≪ 1. Further increasing the Bi number (Bi >1) ultimately results in laminarizing the EVP flow [32,34].

From the literature, it is clear that limited work has been conducted in investigating the role of plasticity on viscoelastic instabilities, specifically, in the limit of negligible inertia (Re ≪ 1). Existing studies have instead focused on investigating the effects of plasticity on inertially driven turbulent flows in the limit of low elasticity (Wi ≪ 1) [31,32,34]. However, it is clear that EVP instabilities likely exist in a large parameter space spanned by three dimensionless parameters, namely, Re, Wi, and Bi. Thus, it remains unclear how plasticity impacts inertialess instabilities in EVP fluids with high elasticity (Wi ≫ 1). Additionally, the conclusions made from previous studies of laminar and turbulent EVP flows have also been drawn from wall-bounded problems, inducing strong shear-dominated flow regimes, such as porous media [35,36,41,42] and channel flow [32,34,37]. To this aim, here we focus on numerically simulating inertialess viscoelastic and EVP instabilities at varying Bi numbers using popular 2D benchmark cases of ET that produce a strong elongational flow regime. We find that the unyielded regions grow with increasing Bi number, whereby the general effect of plasticity appears to gradually suppress the strength of elastic instabilities, providing an avenue to further control inertialess viscoelastic instabilities.

The remainder of this paper is organized as follows. In Sec. II, we define the governing equations and numerical schemes used to describe viscoelastic and EVP flows. In Sec. III, we describe the two popular benchmark cases used to generate an elongational flow regime to transition the flow into inertialess viscoelastic instabilities, as well as the relevant dimensionless parameters. Following this, we present and discuss the results in Sec. IV. eherein we demonstrate the general effect of plasticity on inertialess viscoelastic instabilities in terms of both qualitative and quantitative flow features. Finally, conclusions are drawn, and a future outlook is given in Sec. V.

II. GOVERNING EQUATIONS

We numerically investigate the two-dimensional incompressible flow of viscoelastic and elasto-viscoplastic fluids. Two separate constitutive equations are required to describe the hydrodynamic (i.e., solvent properties) and non-Newtonian (i.e., elastic and plastic properties) fields. The behavior of the solvent can be described through the incompressible Navier-Stokes equations [30],

$$\nabla \cdot \boldsymbol{u} = 0, \quad \rho \frac{D\boldsymbol{u}}{Dt} = -\nabla P + \mu_s \Delta \boldsymbol{u} + \nabla \cdot \boldsymbol{\tau} + \boldsymbol{F}, \tag{1}$$

which is coupled with the the polymer stress tensor $\boldsymbol{\tau} = \frac{\mu_p}{\lambda}(\boldsymbol{C} - \boldsymbol{I})$, described by a space-time-dependent conformation tensor ($\boldsymbol{C}$) constitutive equation,

$$\frac{D\boldsymbol{C}}{Dt} = \boldsymbol{C} \cdot (\nabla \boldsymbol{u}) + (\nabla \boldsymbol{u})^\mathsf{T} \cdot \boldsymbol{C} - \frac{f}{\lambda}(\boldsymbol{C} - \boldsymbol{I}), \tag{2}$$

where ρ is the fluid density, P is the pressure, $\boldsymbol{u}$ is the velocity field, $\boldsymbol{F}$ is the external force, $\boldsymbol{I}$ is the identity tensor, and μ_s and μ_p are the solvent and polymer dynamic viscosities, respectively. Finally, f is an additional term allowing for various constitutive polymer models to be used. Here we consider two cases for f. First, in the case where $f = 1$, Eq. (2) simply reduces to the well-known

Oldroyd-B model [44] and describes the flow of viscoelastic liquids. Specifically, the model predicts only purely elastic polymer effects and is thus useful for modeling constant-viscosity Boger fluids [45]. In the case of EVP flow, we apply the Saramito model [24], such that $f = \max(0, \frac{\tau_d - \tau_0}{\tau_d})$, whereby τ_0 is the yield stress and τ_d is the magnitude of the deviatoric part of the stress tensor, $\boldsymbol{\tau}_d = \boldsymbol{\tau} - \mathrm{tr}(\boldsymbol{\tau})\boldsymbol{I}/2$, that is, $\tau_d = \sqrt{\frac{1}{2}(\boldsymbol{\tau}_d : \boldsymbol{\tau}_d)}$. Based on these two quantities over time, the Saramito model predicts only recoverable Kelvin–Voigt viscoelastic deformation in the unyielded state (i.e., $\tau_d \leqslant \tau_0$), whereas the Oldroyd-B viscoelastic model is retained beyond yielding ($\tau_d > \tau_0$). In the current form, the Saramito model only accounts for the elastic and plastic effects. However, extensions of the model have been made to account for viscous effects, such as shear-thinning [46] and thixotropic behavior [47]. However, here we only apply the general Saramito model described above [24] to simplify the parameter space when investigating the role of plasticity on viscoelastic instabilities with strong elastic effects.

Equations (1) and (2) are solved using a numerical solver comprising of the lattice Boltzmann coupled with a high-order finite-difference scheme (detailed in our previous work [48]), which has been applied in our previous investigations of viscoelastic instabilities [11,12,49–51]. The lattice Boltzmann method (LBM) resolves the hydrodynamic field using a mesoscopic framework, which inherently permits exact advection and is thus devoid of numerical diffusion in Eq. (1). To discretize Eq. (2), we apply a second-order central difference scheme to all spatial gradients. To improve stability and limit the level of numerical diffusion, the polymer solver treats the advection term according to the high-resolution Kurganov-Tadmor scheme [52], while a fourth-order Runge-Kutta scheme is applied for the temporal evolution, whereby any consequent numerical diffusion has been shown to have a negligible effect on accurately depicting viscoelastic instabilities [49,53], retrieving results in direct agreement with previous studies with pseudospectral solvers [48,54–56]. To further enhance numerical stability, we preserve the symmetric-positive-definite property of $\boldsymbol{C}$ [Eq. (2)] by construction by applying the Cholesky decomposition with the positivity enforced through the logarithmic transformation [57]. Finally, an additional Laplace term, $\kappa \Delta \boldsymbol{C}$ is added to the right-hand side of Eq. (2) to stabilize and regulate the buildup of steep polymer stress gradients at high elastic effects through a specified level of artificial diffusivity κ [49,53,55,58,59].

III. PROBLEM DESCRIPTION

In this work, we numerically simulate viscoelastic and elastoviscoplastic fluids in elongational flow regimes that are capable of transitioning the flow into inertialess viscoelastic instabilities. In doing so, two popular cases, namely the four-roll mill (FRM) problem [49,54,55,58] and the cellular forcing (CF) scheme [50,53,60], are applied. The reason for choosing FRM and CF is twofold. On the one hand, both FRM and CF are numerical recreations of popular viscoelastic experimental cases [61–63] that admit the flow to symmetrical rotating and counter-rotating vortices (see Fig. 1). The effect is the generation of well-defined central stagnation points, which allow us to investigae EVP fluids in elongational flow regimes (see Appendix A, whereby the background forcing of FRM is stronger than CF [53]. On the other hand, both cases are renowned benchmark problems for simulating inertialess viscoelastic instabilities, where the flow behavior is well documented for purely viscoelastic fluids [48–50,53,55,58,60], thus facilitating any comparison with EVP fluids.

Both cases are solved in a 2D domain $\boldsymbol{x} = [0, \; n \times 2\pi]^2$ with double periodic boundary conditions (PBCs) where a single unit cell is $[0, 2\pi]^2$. Here n is the level of periodicity, for which $n > 1$ results in n^2 unit cells to be solved. Based on our previous investigations [49,50], FRM with $n = 1$ will result in unphysical artifacts arising from insufficient periodicity, characterized by qualitative anomalies that contaminate the base flow, thus preventing the accurate simulation of viscoelastic instabilities, such as ET. Therefore, we set $n = 2$ for FRM and $n = 1$ for CF (note that additional simulations for CF with $n = 2$ are reported in Appendix C and support the results presented in the main text for $n = 1$). The experimental effect of rollers, which create an elongational flow regime,
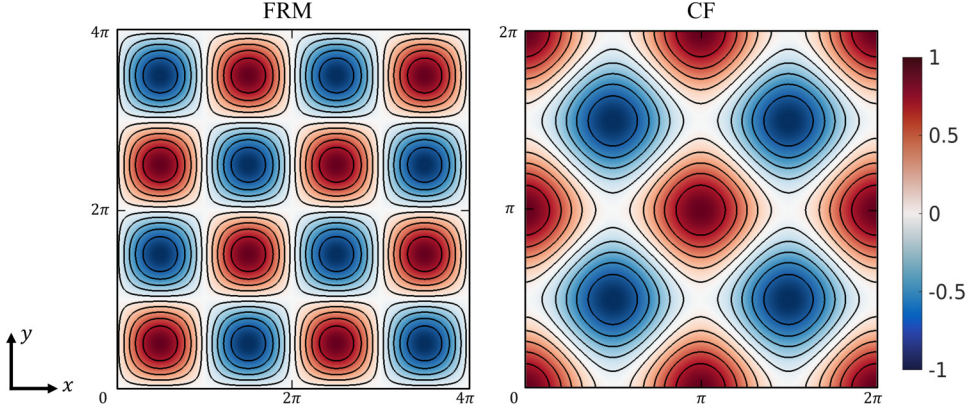
FIG. 1. Normalized vorticity field for the laminar regime in the absence of polymer feedback, for the FRM forcing and CF scheme.

are mimicked through a constant external forcing, which for the FRM problem is given by

$$\boldsymbol{F}(\boldsymbol{x}) = F_0(2\sin(Kx)\cos(Ky), -2\cos(Kx)\sin(Ky)), \tag{3}$$

and for the CF forcing scheme,

$$\boldsymbol{F}(\boldsymbol{x}) = F_0(-\sin(Ky), \sin(Kx)), \tag{4}$$

in which the forcing amplitude is $F_0 = U\nu_s K^2$, where ν_s is the solvent kinematic viscosity, U is the characteristic velocity, and K is the spatial frequency (i.e., $\ell = 1/K$), resulting in a turnover time $T = \nu_s K/F_0$. For FRM (3) $K = 1$ and for CF (4) $K = 2$.

To simulate ET using FRM and CF, a small perturbation $\boldsymbol{\delta}$ is added to the initial conformation tensor $\boldsymbol{C} = \boldsymbol{I} + \boldsymbol{\delta}$, as originally proposed in Ref. [55],

$$\boldsymbol{C}(\boldsymbol{x}, 0) = \boldsymbol{I} + \begin{bmatrix} \delta\cos(Ky)\psi(x) & -\delta\sin(Kx)\cos(2Ky) \\ -\delta\sin(Kx)\cos(2Ky) & \delta\cos(Kx)\psi(y) \end{bmatrix}, \tag{5}$$

with $\delta = 0.01$ and $\psi(z) = 2\sin(Kz) - 3/2\sin(2Kz)$, $z := x, y$.

In all simulations, dimensionless groups are defined following previous numerical investigations of inertialess viscoelastic instabilities using background periodic forcing [49,50,53,55,58,60]. First, we define the relative inertial effects through the Reynolds number, $\mathrm{Re} = F_0/\nu_s^2 K^3$. Here we admit the flow to vanishingly low levels of inertia by setting $\mathrm{Re} = 1$, which is below the critical value at which inertial instabilities arise, $\mathrm{Re}_c = \sqrt{2}$ [64]. To define the behavior of the polymer field, we set the concentration using the parameter, $\beta = \nu_p/\nu_s$, which measures the relative polymer kinematic viscosity, ν_p, to the solvent kinematic viscosity, ν_s. The value $\beta = 0.5$ will be fixed in our simulations to match previous numerical [55,58] and experimental investigations [65]. The relative importance of elastic effects to viscous effects is defined through the Weissenberg number, $\mathrm{Wi} = \lambda/T$, which we set constant to $\mathrm{Wi} = 10$ to simulate viscoelastic instabilities in the limit of high elastic effects [49]. The yield stress criteria of the plastic fluid response is controlled through the Bingham number Bi, which defines the ratio of the yield and viscous stresses, $\mathrm{Bi} = \tau_0/\nu_s UK$. It is clear that when $\mathrm{Bi} \to 0$, a viscoelastic fluid is obtained, whereas $\mathrm{Wi} \to 0$ describes a viscoplastic fluid.

In terms of the numerical setup for both cases, we follow previous investigations [48–50,55,60]. All simulations are conducted with $(n \times N)^2 = 256^2$ grid points, where each unit cell has N^2 grid points, i.e., the resolution $2\pi/N$ for FRM is half of that used for CF. In terms of numerical regulation, we set $\kappa \sim \mathcal{O}(10^{-4})$, so that the Schmidt number, $\mathrm{Sc} = \nu_s/\kappa = 10^3$, matches previous numerical investigations of inertialess viscoelastic instabilities [53,55,58]. Specifically, our previous
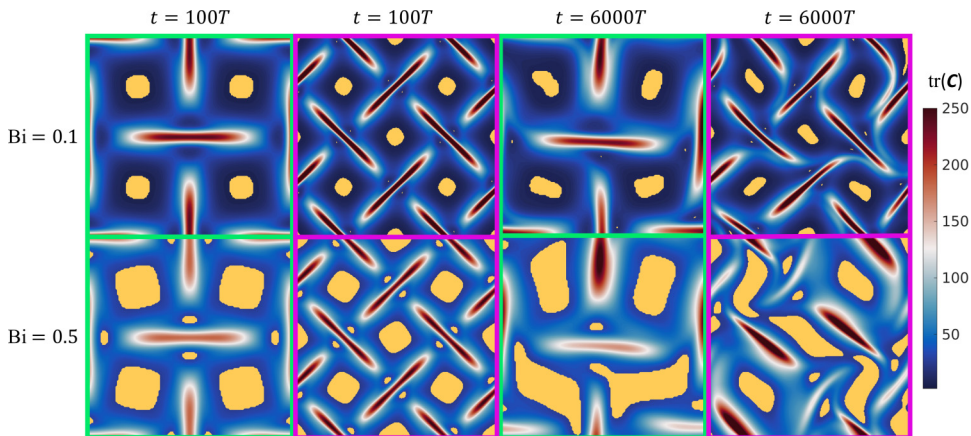
FIG. 2. Representative snapshots of the trace of conformation tensor, tr(C) during the early steady-state ($t = 100T$) and unsteady late stages ($t = 6000T$) for low plasticity (Bi = 0.1) and high plasticity (Bi = 0.5). Superimposed in yellow are the unyielded regions of the flow, where $\tau_d < \tau_0$. Note that green and magenta borders correspond to results obtained for FRM and CF, respectively, over their respective unit cell $[0, 2\pi]$.

investigations of FRM with Sc = 10^3 [49] demonstrated that all features of ET can be retained provided $n \geqslant 2$. Here we note that additional simulations are conducted for CF with higher periodicity ($n = 2$) in Appendix C, which support the results presented in the main text with $n = 1$. Additionally, we further justify the selection of N and κ in Appendix E.

IV. RESULTS AND DISCUSSION

To investigate the effect of plasticity on inertialess viscoelastic instabilities with high elastic effects, we first qualitatively assess the flow behavior. Figure 2 shows representative snapshots of the polymer field through the conformation tensor trace, tr(C), for an EVP fluid at low plasticity (Bi = 0.1) and high plasticity (Bi = 0.5) during the early stages ($t = 100T$) and the late stages ($t = 6000T$) of the flow. Notably, the appearance of unyielded regions (shown in yellow) is observable for both FRM and CF at both Bi numbers. Specifically, during the early steady stages of the flow, the polymer field in both cases is largely confined to the underlying background forcing structure, which develops clear birefringent strands in the vicinity of the central stagnation points that surround the rollers, as previously reported in literature for Wi > 1 and Bi = 0 [49,53–55]. For Bi = 0.1, as expected, the unyielded regions occur in the vortical regions of the flow where polymers rapidly contract [53]. Careful inspection of the results obtained for CF reveals additional small unyielded regions emerging directly above and below the birefringent strands. These regions clearly grow for both FRM and CF at Bi = 0.5 and appear to suppress the relative polymer stretching behavior in the birefringent strands. In the late stages of flow at Bi = 0.1, both cases reflect a minor departure from the initial background forcing symmetry (see also the corresponding movies in the online Supplemental Material [66]); however, the unyielded regions remain mostly confined in the vorticity-dominated areas. During this period, the flow has transitioned into the previously reported viscoelastic instabilities [49,50,53,55,60], characterized by strong time-dependent behavior and minor losses of flow symmetry. Further increasing the plastic effects (Bi = 0.5) causes the unyielded regions to grow and contaminate the base flow. The eventuating symptoms appear to be a more dramatic deviation from the initial flow symmetry, as well as a suppression of time-dependent behavior (see the corresponding movies in the online Supplemental Material [66]).

Qualitative discrepancies between varying Bi cases are not exclusively observed in the polymer field but also appear in the hydrodynamic field. Figure 3 illustrates corresponding vorticity fields
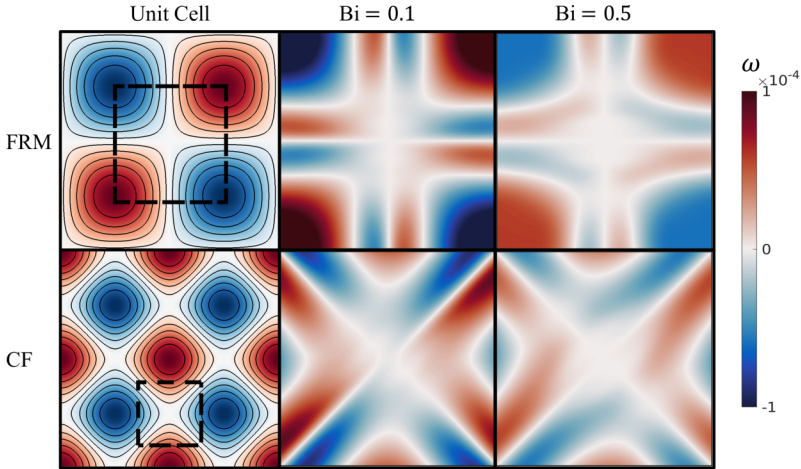
FIG. 3. Representative snapshots of the vorticity field, ω, during the early steady state ($t = 100T$) for low plasticity (Bi = 0.1) and high plasticity (Bi = 0.5). Note that results are illustrated within the vicinity of the central stagnation point for FRM and CF, as represented by the black dashed area within their respective unit cell $[0, 2\pi]$.

in the early stages of the flow ($t = 100T$) for Bi = 0.1 and Bi = 0.5. As the yield criteria become more strict and the unyielded regions grow, the strength of the vorticity field in the direct vicinity of the central stagnation points appears to become weaker. Notably, the zero-vorticity regions that emerge as Bi increases directly coincide with the unyielded regions that develop near the polymer birefringent strands in Fig. 2. The strength of the counter-rotating vortices that develop due to the background forcing is indeed an essential ingredient for driving inertialess viscoelastic instabilities [4,53,55,58]. In what follows, we will demonstrate the implications of suppressing these vortical regions, specifically in terms of the transition and strength of viscoelastic instabilities that develop.

Figure 4 shows the FRM results for the time series of the first component of the conformation tensor C_{xx} at the central stagnation point position, $[\pi, \pi]$, for different Bi numbers. For the purely viscoelastic case (Bi = 0), the flow transitions from a laminar steady-state solution into strong time-dependent flow fluctuations at $t \approx 500T$, as previously observed for FRM [49,55,58]. Imposing a small but finite yield stress criterion (Bi = 0.05) results in the emergence of a new flow regime prior to the transition into aperiodic flow fluctuations. Specifically, a small window of quasiperiodic fluctuations develops, which qualitatively represents the polymer field regularly switching between distinct flow states due to the emergence of dominant vortices (see the corresponding movies in the online Supplemental Material [66]). Similar flow behavior has been previously observed using the FRM for purely viscoelastic fluids (Bi = 0) [49,50,55,58], wherein the quasiperiodic dynamics where labeled as numerical artefacts eventuating from the combined effect of insufficient periodicity ($n < 2$) and global artificial diffusivity. Here we stress that in our simulations of FRM with $n = 2$, we do not observe quasiperiodic flow behavior at Bi = 0, but only on imposing a yield stress criteria (Bi > 0), thus likely reflecting a physically sourced origin as opposed to a numerical artefact. Further increasing the plastic tendency of the EVP fluid generally causes the quasiperiodic fluctuations to span a longer period of time. However, there are notable examples which allude to a more complex underlying phenomena, wherein the transition between different flow states does not appear in an expected linear fashion on increasing Bi. Such examples are evident in Fig. 4 between Bi = 0.1 and Bi = 0.15, as well as between Bi = 0.2 and Bi = 0.3, whereby on increasing Bi, the localized periodic fluctuations in both cases occur over a shorter time span. It is also noticeable that gradually increasing the Bi number causes the quasiperiodic fluctuations (i.e., Bi = 0.1) to obtain a more periodic behavior (i.e., Bi = 0.2) before eventually disappearing altogether
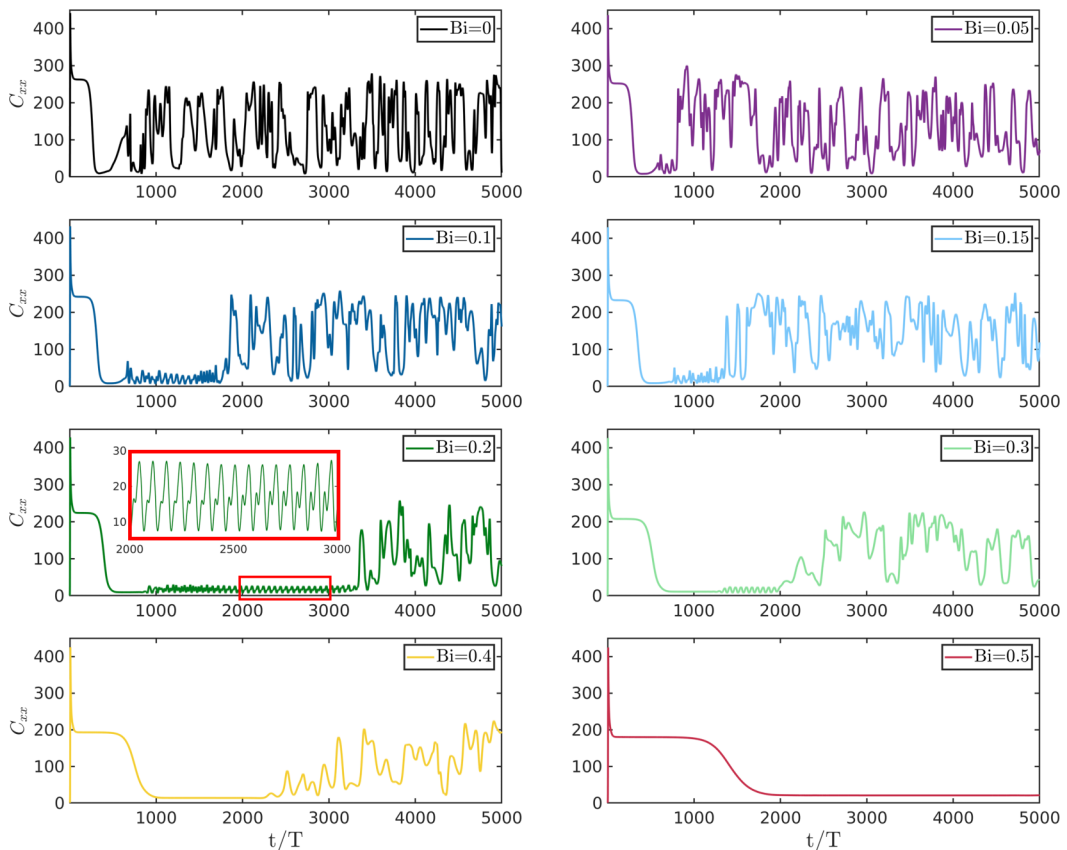
FIG. 4. Time series of the first component of the conformation tensor C_{xx} for FRM at the position $[\pi, \pi]$ taken over $0 \leqslant t/T \leqslant 5000$. Results are compared at different Bi numbers, namely Bi = 0 (black), Bi = 0.05 (purple), Bi = 0.1 (dark blue), Bi = 0.15 (light blue), Bi = 0.2 (dark green), Bi = 0.3 (light green), Bi = 0.4 (yellow), and Bi = 0.5 (red). Note the inset in the subplot corresponding to Bi = 0.2 illustrates a zoomed-in snapshot of the periodic regime.

(i.e., Bi = 0.4). Notably, the observed periodic orbits are highly sensitive to the underlying flow conditions, specifically, the interplay between elastic and plastic effects, as shown in Appendix D. In terms of the dynamics observed in the late stages of the flow, the purely viscoelastic case (Bi = 0) experiences chaotic high-frequency flow fluctuations, which appear to become slower and eventually disappear as Bi is increased.

Analogous results are obtained for CF in Fig. 5, which show similar flow behavior. Specifically, three distinct flow regimes also emerge as the Bi number is gradually increased (i.e., laminar, periodic, and aperiodic). However, the periodic orbits that appear for CF at Bi $\geqslant 0.1$ are characterized by higher-frequency oscillations and qualitatively represent the periodic circulation of vortices, which cause the polymer birefringent strands to rapidly stretch and contract in the strain-dominated regions (see the corresponding movies in the online Supplemental Material [66]). The time taken to overcome the periodic orbits and transition into the fully developed viscoelastic instability also appears to follow a more linear trend as Bi increases. Akin to FRM, the aperiodic fluctuations in the late stages of the flow for CF also appear to decrease and eventually laminarize as Bi increases. Notably, we have conducted additional simulations for CF with $n = 2$ (see Appendix C, which confirm the results obtained with $n = 1$ in Fig. 5.
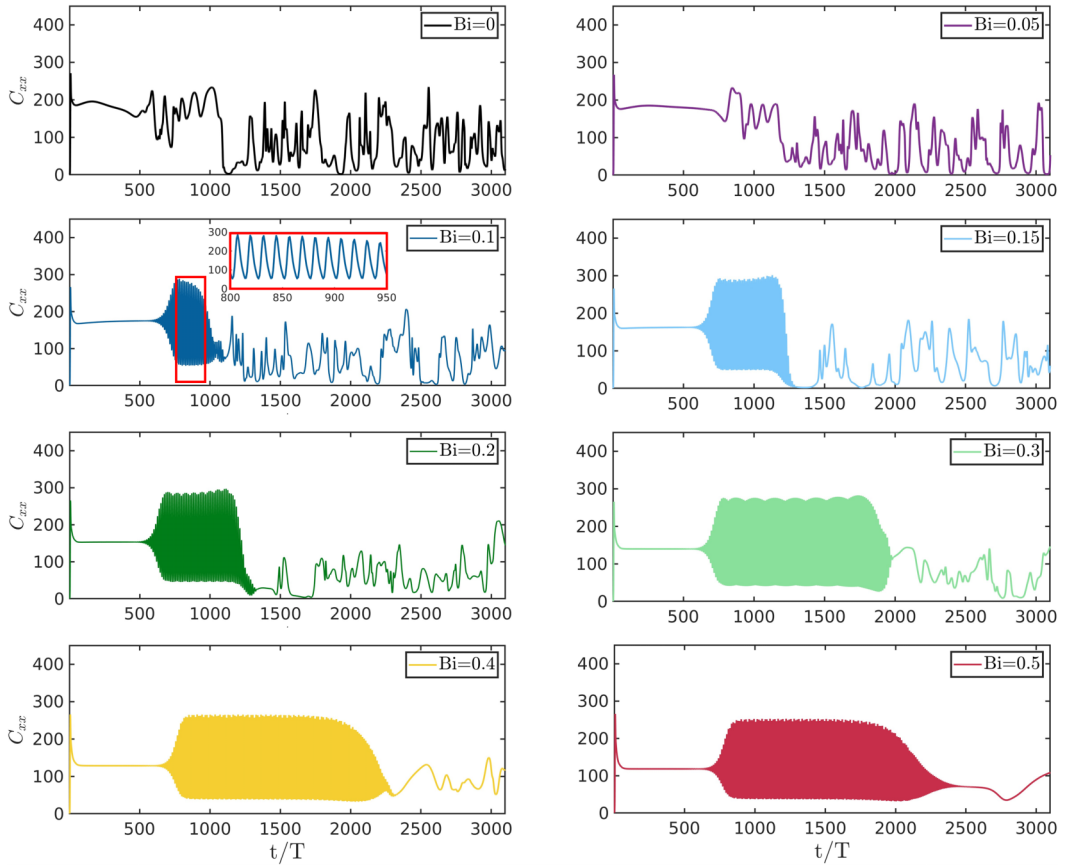
FIG. 5. Time series of the first component of the conformation tensor C_{xx} for CF at the position $[\pi/2, \pi]$ taken over $0 \leqslant t/T \leqslant 3000$. Results are compared at different Bi numbers, namely Bi $= 0$ (black), Bi $= 0.05$ (purple), Bi $= 0.1$ (dark blue), Bi $= 0.15$ (light blue), Bi $= 0.2$ (dark green), Bi $= 0.3$ (light green), Bi $= 0.4$ (yellow), and Bi $= 0.5$ (red). Note, the inset in the subplot corresponding to Bi $= 0.1$ illustrates a zoomed-in snapshot of the periodic regime.
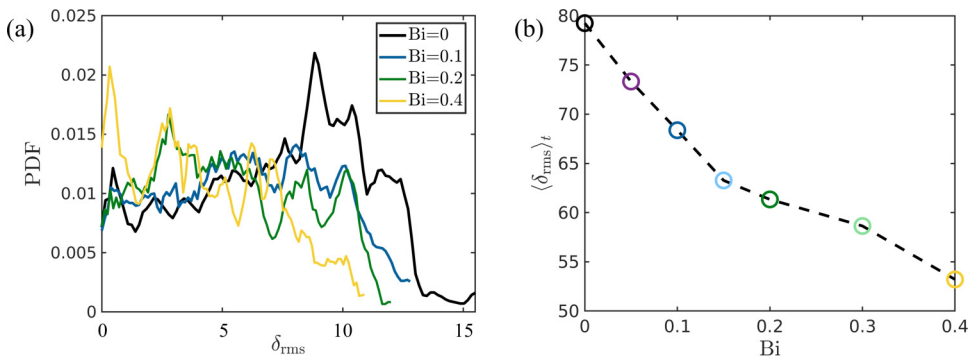
FIG. 6. Characterization of the flow fluctuations during the late stages of the flow for FRM: (a) The probability density function (PDF) of the local temporal flow fluctuations, δ_{rms}, for different Bi numbers. (b) The temporally averaged flow fluctuations, $\langle \delta_{\mathrm{rms}} \rangle_t$, which monotonically decreases with Bi.

We further characterize the behavior during the late stages of the flow for FRM in Fig. 6. More specifically, we compute the local temporal fluctuations, $\delta_{\mathrm{rms}} = \sqrt{[C_{xx}(\pi, \pi, t) - \langle C_{xx}(\pi, \pi, t) \rangle_t]^2}$, of the polymer field over a sample of $1000T$ in the statistically homogeneous regime. Figure 6(a) shows the probability density function (PDF) of δ_{rms} for different Bi numbers, wherein the purely viscoelastic case (Bi $= 0$) retains a broad range of fluctuations, the majority of which occur in the upper limit ($\delta_{\mathrm{rms}} > 8$). On gradually increasing Bi, the solidlike behavior of the EVP fluid tends to suppress the level of fluctuations in C_{xx}. This is especially noticeable for Bi $= 0.4$, which is instead predominantly characterized by small fluctuations, such that $\delta_{\mathrm{rms}} < 5$. The temporally averaged behavior, $\langle \delta_{\mathrm{rms}} \rangle_t$, in Fig. 6(b) further demonstrates that as the solidlike tendency of the EVP fluid increases with Bi, the level of fluctuations monotonically decreases. Analogous results are obtained for CF in Appendix B, which draw the same conclusions. Notably, it is worth mentioning that the FRM case exhibits stronger flow fluctuations compared to CF. As previously mentioned, this tendency can be attributed to the inherently stronger background forcing of FRM [53].

To further assess the impact of plasticity on the late stages of the flow, specifically, the frequency of oscillations f, Fig. 7 compares the continuous Morlet wavelet transform of C_{xx} for different Bi numbers using FRM. The purely viscoelastic case (Bi $= 0$) is characterized by highly temporal behavior, appearing to activate a broad range of frequencies in the limit $0 \leqslant f \leqslant 1$. For the EVP fluid with Bi $= 0.1$, the emergence of unyielded regions appears to suppress some of the transient nature of the viscoelastic instability and is not able to recover the full range of frequencies. This effect becomes even more observable for Bi $= 0.2$, as the higher-frequency oscillations in C_{xx} do not occur constantly but instead in intervals over time. Further increasing the plasticity (Bi $= 0.4$), almost completely suppresses the strength and range of oscillations, as well as the intermittency. Notably, this behavior is different from previous observations involving the flow of EVP fluids in shear-dominated flow regimes, such as channel flow [32,34,67], wherein intermediate plastic effects (Bi ~ 1) contributed to enhanced flow fluctuations and intermittency, resulting from the dynamic yielding and unyielding process in the center of the channel. Here, however, the general effect of plasticity appears to monotonically suppress and laminarize the inertialess viscoelastic instabilities that develop in elongational flow regimes.

We further quantify the type of flow developed in FRM and CF and its effect on the unyielded regions by computing the flow topology parameter (also commonly referred to as the "flow-type parameter"),

$$Q = \frac{||\boldsymbol{D}|| - ||\boldsymbol{\Omega}||}{||\boldsymbol{D}|| + ||\boldsymbol{\Omega}||}, \tag{6}$$

which categorizes the local flow kinematics in terms of pure rotation ($Q = -1$), simple shear ($Q = 0$), and pure extension ($Q = 1$), where $\boldsymbol{D} = \frac{1}{2}(\nabla \boldsymbol{u} + \nabla \boldsymbol{u}^{\mathsf{T}})$ and $\boldsymbol{\Omega} = \frac{1}{2}(\nabla \boldsymbol{u} - \nabla \boldsymbol{u}^{\mathsf{T}})$ correspond to the strain rate and vorticity tensors, respectively, with $||\boldsymbol{D}|| = \sqrt{2\boldsymbol{D} : \boldsymbol{D}}$ and $||\boldsymbol{\Omega}|| = \sqrt{2\boldsymbol{\Omega} : \boldsymbol{\Omega}}$. Figure 8(a) illustrates that in the early steady-state stages ($t = 200T$) for both cases, the flow remains unyielded predominantly in the rotational regions of the flow, as illustrated in the qualitative snapshots from Fig. 2. Notably, a small portion of the flow is also unyielded in the elongational regions, which correspond to the unyielded regions illustrated near the birefringent strands in Fig. 2. As the Bi number increases, a larger portion of the flow surrounding the birefringent strands remains unyielded [refer to the inset B in Fig. 8(a)]. Similar behavior is observed in the late stages of the flow ($t = 5000T$) in Fig. 8(b), as the effect of plasticity appears to decrease the quantity of unyielded regions induced by rotational effects while increasing the unyielded regions developed by strong elongational effects. Qualitatively, this behavior corresponds to the unyielded regions that grow and contaminate the base flow in Fig. 2, provided Bi > 0.1.

Thus far, certain discrepancies have been highlighted between the results obtained for FRM and CF. These include the difference in transitioning times between the distinct flow states observed in Figs. 4 and 5, as well as the contrasting behavior within the periodic regime. To further investigate
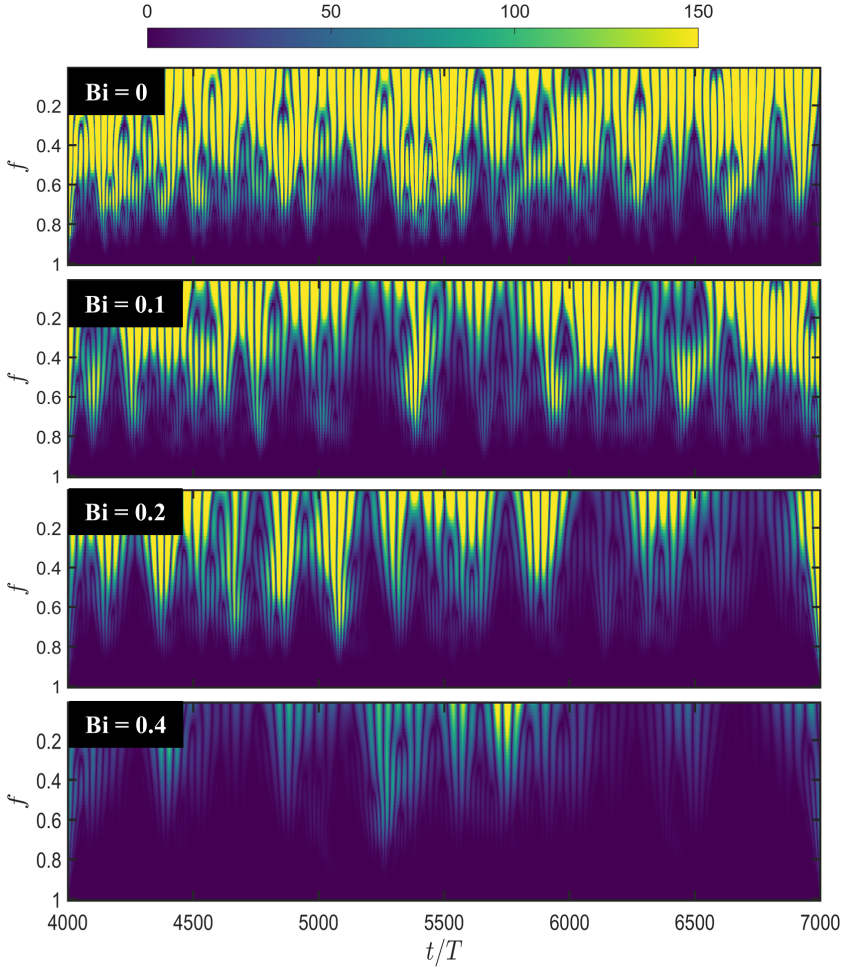
FIG. 7. The continuous Morlet wavelet transformation of C_{xx} with FRM at the position $[\pi, \pi]$ taken over the late stages of the flow, $4000 \leqslant t/T \leqslant 7000$. Results are compared at different Bi numbers: (from top to bottom) Bi $= 0, 0.1, 0.2$, and 0.4.

these discrepancies, we conduct a statistical binary analysis of the unyielded regions $\boldsymbol{F}(\boldsymbol{x}, t)$, where $\boldsymbol{F} = 1.0$ when $\tau_d(\boldsymbol{x}, t) \leqslant \tau_0$; otherwise, $\boldsymbol{F} = 0.0$. In particular, we compute the temporal average, $\Lambda(\boldsymbol{x}) = \langle \boldsymbol{F}(\boldsymbol{x}, t) \rangle_t$. Figure 9 plots the corresponding contour for $\Lambda(\boldsymbol{x})$ in the periodic regime with temporally averaged contour lines $\langle \text{tr}(\boldsymbol{C}) \rangle_t$ at different Bi numbers. Immediately observable is the loss of initial flow symmetry for FRM, whereby distinct vortical regions are lost, and polymer stretching becomes biased towards the longitudinal direction. In this periodic regime, the unyielded regions are located in the vicinity of the polymer birefringent strands. On close visual inspection, it is clear that making the yield stress criteria more stringent from Bi $= 0.1$ to Bi $= 0.15$ increases the total number of sites that become unyielded over time. However, further increasing the plastic effects (Bi > 0.15) appears to instead gradually localize the total number of unyielded regions, specifically, becoming more concentrated directly above and below the longitudinally stretched polymers. The quantitative results in Figure 10(a) further support this finding by computing the ratio of the domain N^2 that is unyielded through the parameter $\tilde{\Lambda} = \frac{|\{k : \Lambda(x_k) > 0\}|}{N^2}$, where ":" denotes the set formed by the unyielded values of k and "$|\cdot|$" represents the cardinality. The increasing values in $\tilde{\Lambda}$ observed for CF with growing plasticity represent an expanding spatial dispersion of unyielded regions over time,
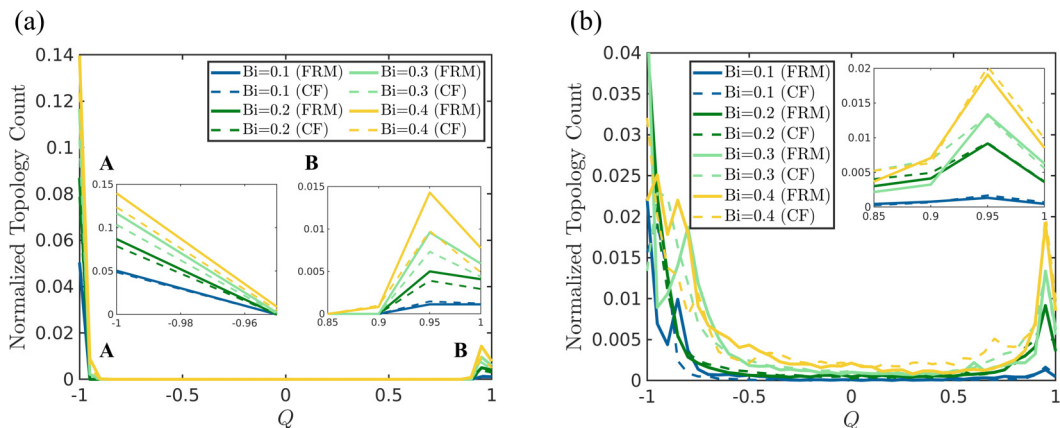
FIG. 8. Representative histogram for the unyielded regions and their corresponding flow topology parameter, Q, during the (a) early steady-state ($t = 200T$) and (b) aperiodic regime ($t = 5000T$) for different Bi numbers. Note that the FRM and CF results are represented by solid and dashed lines, respectively. The insets in (a) are the zoomed-in results for the rotational (region A) and elongational (region B) flow regimes. The inset in (b) corresponds to zoomed-in results for the elongational flow regime.

whereas the decreasing values in $\tilde{\Lambda}$ for FRM as Bi > 0.15 reflect a more concentrated system. In terms of the normalized spatial average, we compute $\langle\Lambda\rangle_{F>0}$, which reflects the average residence of unyielded regions in the system. Figure 10(b) illustrates the existence of a critical transitioning point for FRM at $0.15 <$ Bi < 0.2, wherein the results remain unchanged in $\langle\Lambda\rangle_{F>0}$ for Bi $\leqslant 0.15$ and suddenly increase for Bi >0.15, which qualitatively is reflected by the emergence of concentrated regions in Λ directly above and below the longitudinally stretched polymers (refer to Fig. 9).

On the other hand, for the CF results in Fig. 9, the initial forcing symmetry is retained over time in the periodic regime for all Bi numbers. As a result, the unyielded regions that develop follow
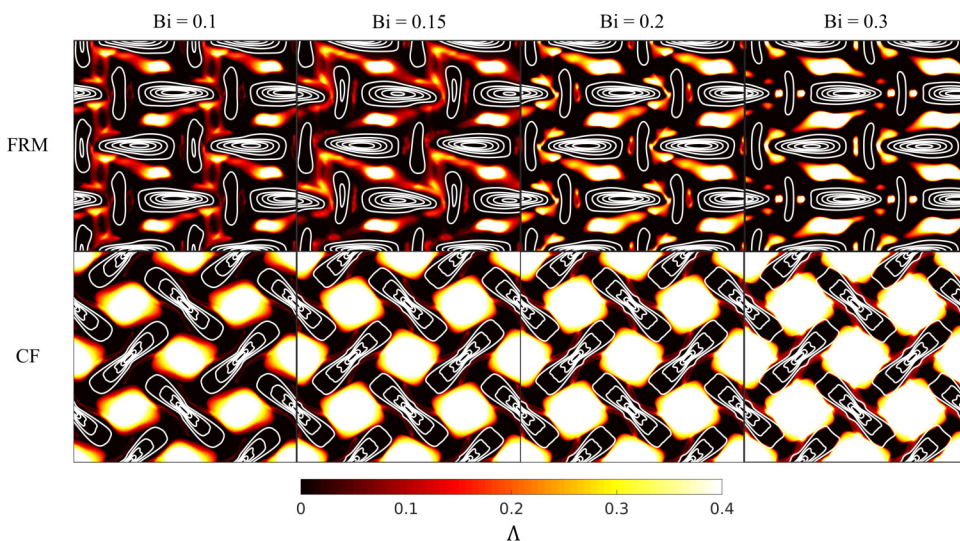
FIG. 9. Contour plots for Λ, sampled over a window of $300T$. Results are illustrated for FRM (top row) and CF (bottom row) at (from left to right) Bi $= 0.1, 0.15, 0.2$, and 0.3. Superimposed in white are the corresponding temporally averaged conformation tensor trace, $\langle\text{tr}(\boldsymbol{C})\rangle_t$, contour lines.
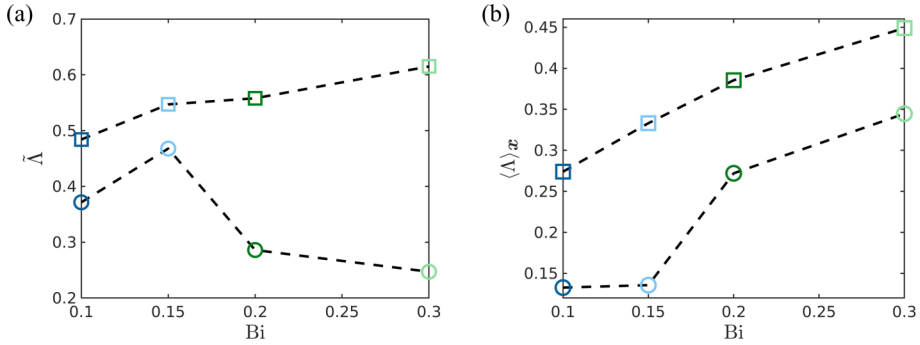
FIG. 10. Characterization of the unyielded regions in the periodic regime at different Bi numbers. (a) The total dispersion of unyielded regions over time, as represented by $\tilde{\Lambda}$. (b) The normalized spatial average, $\langle \Lambda \rangle_{F>0}$. Results are obtained for both FRM (circles) and CF (squares). Notably, the results in CF follow a monotonic trend, whereas the FRM results are less trivial.

a more predictable behavior with increasing Bi numbers. Qualitatively, the unyielded locations are primarily contained within the vortical regions of the flow. Increasing Bi appears to simultaneously enlarge the total number of locations within the vortical regions that become unyielded over time [Fig. 10(a)], as well as the average number of unyielded instances [Fig. 10(b)]. These unyielded regions appear to be responsible for the high-frequency periodic fluctuations in CF, which act to delay the transition into aperiodic fluctuations with increasing Bi numbers (refer to Fig. 6). Overall, the results further demonstrate the complex and nontrivial flow behavior that emerges in the periodic flow state for FRM, which can be attributed to the unyielded flow regions that arise and destroy the initial background forcing symmetry.

In the aperiodic late stages of the flow, both the FRM and CF cases largely conform to the same flow behavior (Figs. 11 and 12), i.e., increasing Bi, and hence the solidlike tendencies of the EVP
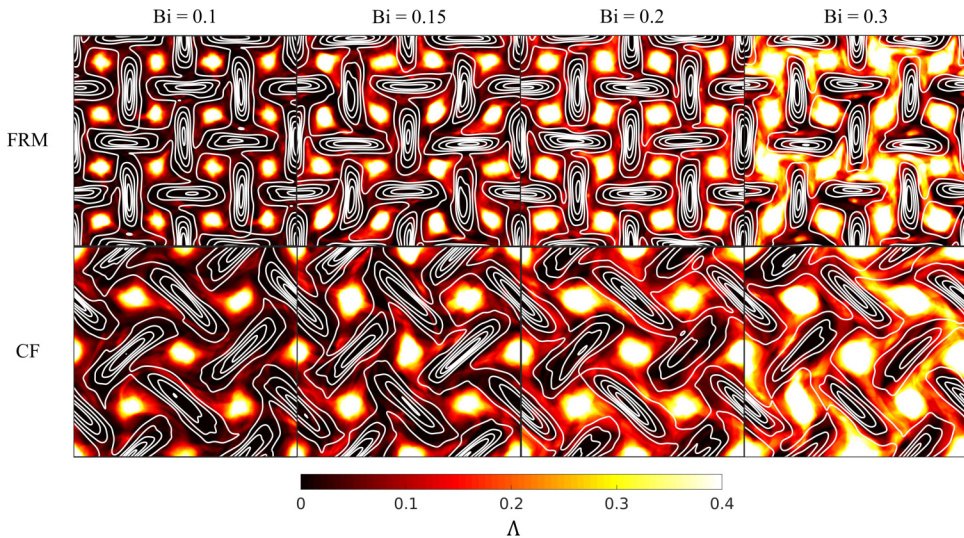
FIG. 11. Contour plots for Λ in the aperiodic late stages of the flow, sampled over a window of $1000T$. Results are illustrated for FRM (top row) and CF (bottom row) at (from left to right) Bi $= 0.1, 0.15, 0.2$, and 0.3. Superimposed in white are the corresponding temporally averaged conformation tensor trace, $\langle \text{tr}(\boldsymbol{C}) \rangle_t$, contour lines.
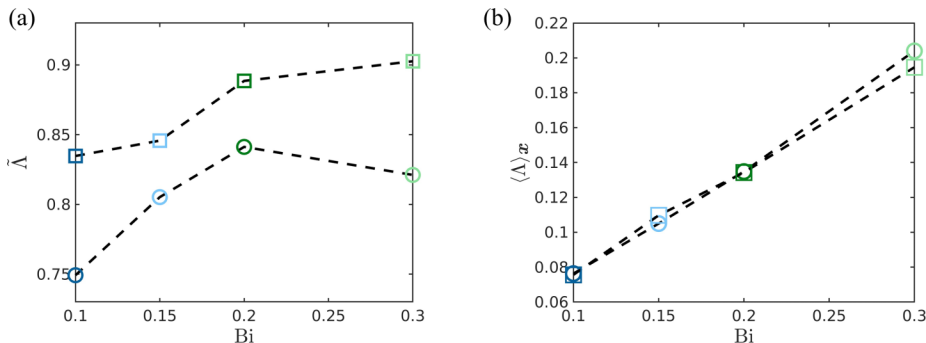
FIG. 12. Characterization of the unyielded regions in the aperiodic late stages of the flow at different Bi numbers. (a) The total dispersion of unyielded regions over time, as represented by $\tilde{\Lambda}$. (b) The normalized spatial average, $\langle \Lambda \rangle_{F>0}$. Results are obtained for both FRM (circles) and CF (squares). Notably, both cases conform to similar flow behavior in the late stages of the flow.

fluid suppress the strength of the fully developed viscoelastic instability (refer to Figs. 6 and 7, as well as Appendix B. Figure 11, which illustrates the contour plots for Λ, provides an avenue for explaining this shared similarity. More specifically, it is noticeable that within the late stages, both FRM and CF mostly recover the initial background forcing symmetry, resulting in the emergence of unyielded points predominantly within the vortical regions of the flow. However, as the yield stress criteria (Bi) becomes more strict, additional unyielded locations emerge, which surround the polymer birefringent strands. This is further reflected in Fig. 12(a), which shows a large increase in $\tilde{\Lambda}$ by gradually incrementing the plastic effects in the limit, $0.1 \leqslant \text{Bi} \leqslant 0.2$.

Notably, when $\text{Bi} > 0.2$, a diminishing value in $\tilde{\Lambda}$ is observed for both cases, corresponding to a minor loss of flow symmetry evident in Fig. 11. This asymmetry is a persistent effect following the initial transition into flow asymmetry and transient flow behavior, appearing to arise specifically in EVP cases where solidlike tendencies prevail, delaying the recovery of the initial background forcing symmetry (refer to the online Supplemental Material [66]). This effect appears to be more dominant for FRM, whereby certain polymer birefringent strands, illustrated by the white contour lines, appear to be unevenly stretched, resulting in small regions that yield directly above or below longitudinally stretched polymers. In terms of the average unyielded flow states, $\langle \Lambda \rangle_{F>0}$, Fig. 12(b) shows that the results obtained for both FRM and CF collapse onto the same trend. That is, in the statistically homogeneous regime, the normalized average quantity of unyielded points is approximately the same for both cases across different Bi numbers. This shared behavior is largely expected given that unlike with the periodic regime in Fig. 9, both cases in Fig. 11 retain the same vortical geometry in the aperiodic regime. Thus, the smaller flow fluctuations observed for CF in the late stages of the flow (refer to Appendix B are likely attributed to the more widespread distribution of unyielded locations over time, specifically, those surrounding the polymer birefringent strands.

V. CONCLUSIONS

Non-Newtonian fluids possess several nonlinear material properties, which can give rise to interesting time-dependent flow instabilities not experienced in purely Newtonian fluids [4]. In this work, we investigate a subclass of non-Newtonian fluids, EVP fluids, which simultaneously possess viscous, elastic, and plastic properties, giving rise to both solid and fluidlike tendencies depending on the yield stress criterion. Specifically, we conduct numerical simulations of viscoelastic and EVP fluids by integrating the Saramito model [24] into our previously developed hybrid lattice Boltzmann model [48,51]. In contrast to previous studies of flow instabilities with EVP fluids, which have focused on wall-bounded shear flow problems [32,34–36,42,67], here we conduct simulations for benchmark cases that admit strong elongational effects, namely FRM and CF, wherein we focus

on investigating the effects of plasticity (Bi) on viscoelastic instabilities originating from Boger fluids (i.e., constant viscosity) in the limit of vanishingly small inertial effects (Re $\sim$ 1) and high elastic effects (Wi = 10).

In our study, we demonstrate the emergence of three distinct flow states over time, which strongly depend on the Bi number, namely a laminar steady state, periodic orbits, and an eventual transition into aperiodic fluctuations in the late stages. The problem is well defined for Bi $<$ 0.1 cases for both the FRM and CF background forcing structures, with unyielded regions predominantly occurring in the vortical regions of the flow. However, further increasing the solidlike tendencies of the EVP fluid (Bi $>$ 0.1) is shown to promote unyielding in the extension-dominated areas surrounding the polymer birefringent strands, reflecting a decrease in the vorticity magnitude. Beyond this initial stage, for certain Bi numbers and depending on the benchmark case (FRM or CF), the flow transitions into a regime characterized by high-frequency periodic fluctuations. For FRM, these periodic orbits emerge for only intermediate plastic effects ($0.05 \leqslant$ Bi $\leqslant 0.3$) and disappear in the two extremities of purely viscoelastic flow (Bi = 0) and when the EVP fluid approaches viscoplasticity (Bi $>$ 0.3). Moreover, the time of onset and duration of the periodic regime occur in a nonlinear manner with increasing Bi. In the case of CF, strong periodic orbits develop beyond Bi $\geqslant 0.1$ and appear to gradually delay the transition into the fully developed viscoelastic instability as Bi increases. Contrasting results between FRM and CF were attributed to the vastly different unyielded behavior in the periodic regime. For different Bi numbers, the FRM case leads to flow asymmetry, wherein well-defined vortical structures are lost and unyielded regions surround longitudinally stretched polymers. The effect is a nonmonotonic trend in the dispersion and average quantity of unyielded points over time with increasing Bi number. On the other hand, during the periodic orbits, the CF polymer field retains forcing symmetry, where large portions of the domain remain unyielded exclusively in the vortical regions. Increasing the plastic effects only further increases the unyielded vortical regions, thus delaying the transition into fully developed viscoelastic instability.

In the late stages of the flow, both FRM and CF mostly conform to similar flow behavior at varying Bi numbers. With increasing plasticity, the unyielded regions grow outside of the vortical regions and contaminate the base flow, restricting the motion of polymer birefringent strands. The result is a suppression of the polymer feedback effects, which decreases the strength and frequency range of flow fluctuations. That is, the effect of increasing plasticity on fully developed viscoelastic instabilities that eventuate from inertialess elongational flow regimes is to suppress and laminarize their behavior, thus allowing for a potential avenue to control their effects.

The analysis performed here only considers the effect of varying Bi at fixed elastic effects (Wi = 10) and omits any shear-thinning effects. It is clear that instabilities arising in EVP fluids likely exist in a large parameter space spanned by three dimensionless parameters, namely, Re, Wi, and Bi. Future studies should, therefore, focus on exploring how these competing effects simultaneously impact inertialess viscoelastic instabilities. Furthermore, the results show that even for two identical elongation-driven benchmark cases, the plastic response resulting from EVP fluids can significantly alter the underlying flow behavior. The elongational flow regimes simulated in this work with FRM and CF are just two of several potential flow types [4] that allow investigating EVP fluids beyond previously explored shear-dominated problems.

APPENDIX A: FLOW TOPOLOGY CHARACTERIZATION

The numerical results presented in the main text were obtained from popular benchmark cases of viscoelastic instabilities, namely FRM and CF. A characteristic feature of these cases is their ability

(a)

(b)
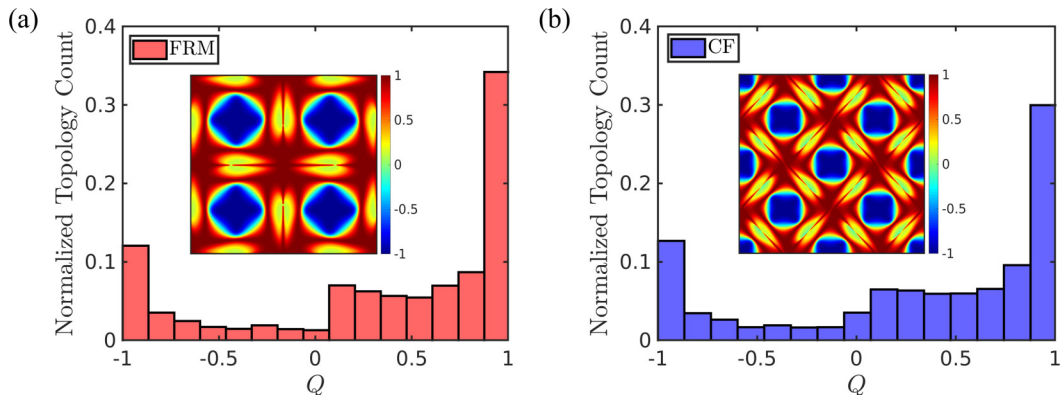
FIG. 13. Flow topology parameter Q histogram during the early stages of the flow ($t = 100T$) for (a) FRM and (b) CF. The insets in (a) and (b) correspond to contour plots for Q. Note that the results demonstrate the elongational nature of the benchmark cases.

to generate an extension-dominated flow regime through multiple rotating and counter-rotating rollers [49,53–55]. To demonstrate this, we compute the flow topology parameter, Q, using Eq. (6). The corresponding results in Fig. 13, show that both FRM and CF reflect an elongational flow regime. More specifically, the strong rotational flow regions, which directly coincide with the placement of rollers, generate strong elongational effects, especially at the central stagnation points, as well as shear flow directly in the locations surrounding the rollers.

APPENDIX B: FLOW FLUCTUATIONS FOR THE CELLULAR FORCING SCHEME

In this section of the Appendix, we present analogous results to Fig. 6 in the main text but for CF. The results in Fig. 14(a) also demonstrate that for CF, increasing the solidlike behavior of the EVP fluid suppresses the strength of flow fluctuations in the late stages of the flow. This is further supported in Fig. 14(b), which shows that the temporally averaged fluctuations, $\langle \delta_{\mathrm{rms}} \rangle_t$, monotonically decrease as Bi increases. Overall, the results obtained with CF confirm that the

(a)

(b)
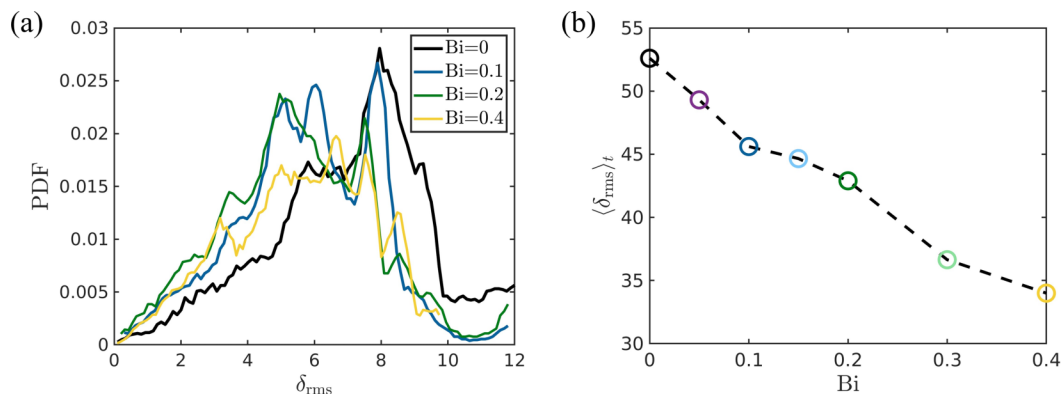
FIG. 14. Characterization of the flow fluctuations during the late stages of the flow for CF. (a) The PDF of the local temporal flow fluctuations, δ_{rms}, for different Bi numbers. (b) The temporally averaged flow fluctuations, $\langle \delta_{\mathrm{rms}} \rangle_t$, which monotonically decreases with Bi.
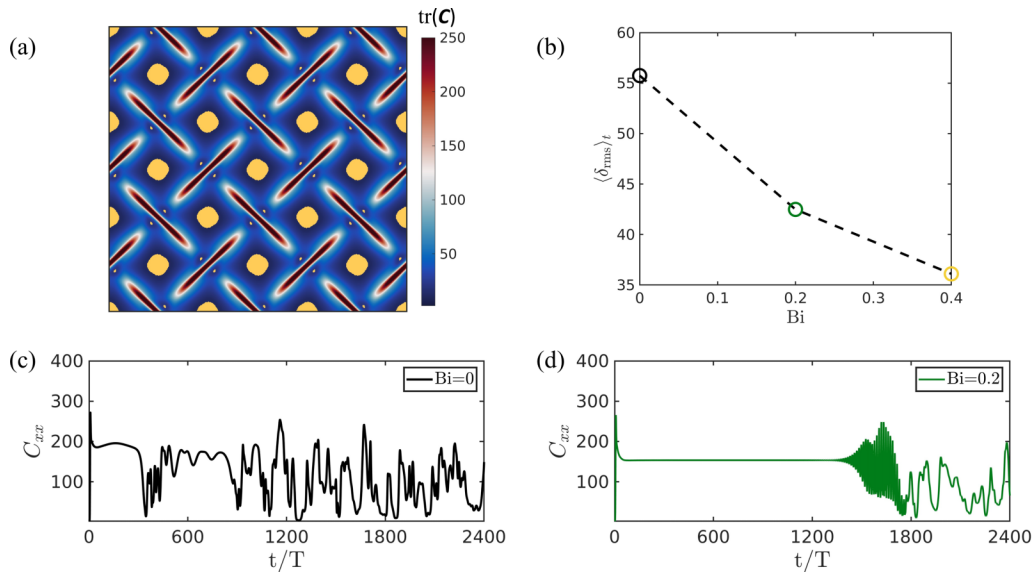
FIG. 15. Results for CF using $n = 2$; (a) a snapshot of $\mathrm{tr}(\boldsymbol{C})$ during the early steady state ($t = 100T$) for low plasticity (Bi = 0.1). Superimposed in yellow are the unyielded regions of the flow, where $\tau_d < \tau_0$. (b) The temporally averaged flow fluctuations, $\langle\delta_{\mathrm{rms}}\rangle_t$, which monotonically decreases with Bi. [(c) and (d)] The time series of C_{xx} at the position $[\pi/2, \pi]$ taken over $0 \leqslant t/T \leqslant 2400$ for Bi = 0 (black) and Bi = 0.2 (dark green), respectively.

conclusions drawn from the main text are not specific to FRM but instead appear to generally apply to extension-dominated problems with periodic background forcing.

APPENDIX C: HIGHER PERIODICITY RESULTS FOR THE CELLULAR FORCING SCHEME

In this section of the Appendix, we perform analogous simulations using CF with $n = 2$. The results in Fig. 15 demonstrate that on increasing the level of periodicity, the same qualitative and quantitative features are retrieved. Specifically, Fig. 15(a) shows the same steady-state behavior in polymer field for Bi = 0.1, whereby unyielded regions develop in the vortical regions, as well as near the birefringent strands, as observed in the main text for CF with $n = 1$ (refer to Fig. 2). The time-dependent behavior for viscoelastic [Fig. 14(c)] and EVP [Fig. 15(d)] fluids also supports the results from the main text (Fig. 5), ehereby the solidlike tendencies of the EVP fluid transition the flow into periodic orbits before the fully developed viscoelastic instability. Moreover, the aperiodic fluctuations in the late stages of the flow are suppressed and become weaker as the Bi number increases [Fig. 15(b)].

APPENDIX D: EFFECT OF THE WEISSENBERG NUMBER ON ELASTOVISCOPLASTIC SIMULATIONS

In the main text, a unique feature of increasing the Bi number involves transitioning the flow dynamics into periodic orbits for both FRM and CF. In this section of the Appendix, we investigate
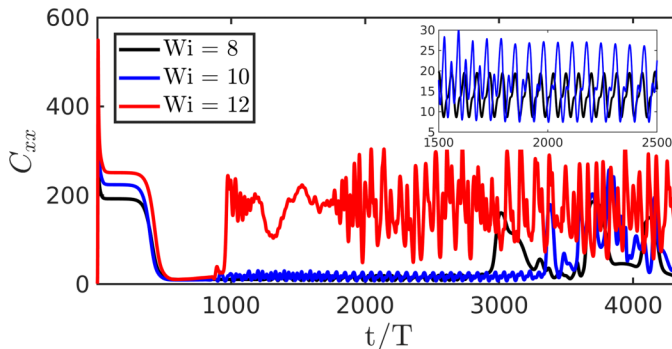
FIG. 16. Time series of the first component of the conformation tensor C_{xx} for FRM at the position $[\pi, \pi]$. Results are compared at Bi $= 0.2$ for different Wi numbers, namely Wi $= 8$ (black), Wi $= 10$ (blue), and Wi $= 12$ (red). The inset corresponds to a zoomed-in snapshot of the periodic regimes for Wi $= 8$ and Wi $= 10$.

the uniqueness and sensitivity of the periodic orbits on the simulation parameters by conducting additional simulations for FRM at Bi $= 0.2$ with varying elastic effects, namely Wi $= 8$, Wi $= 10$, and Wi $= 12$ (Fig. 16). The results for Wi $= 12$ in Fig. 16, clearly demonstrate that the periodic orbits are indeed sensitive to the competing levels of elasticity and plasticity, whereby, increasing the Wi number generally appears to decrease the strength and duration of periodic fluctuations. However, when directly comparing the results for Wi $= 8$ and Wi $= 10$, the duration of periodic fluctuations is slightly longer for Wi $= 10$, which also posses a higher amplitude. The subsequent fluctuations in the late stages for all cases become more chaotic as Wi increases, further supporting the main conclusions from the investigation, that is, inertialess EVP instabilities induced by elongational flow regimes are driven by purely elastic effects.

APPENDIX E: GRID REFINEMENT AND ARTIFICIAL DIFFUSIVITY

To justify the choice of simulation parameters from the investigation, we have conducted a grid refinement study, as well as additional test cases where we vary the level of artificial diffusivity through Sc. In Fig. 17(a), it is clear that an unresolved grid resolution [i.e., $(n \times N)^2 = 128^2$] is
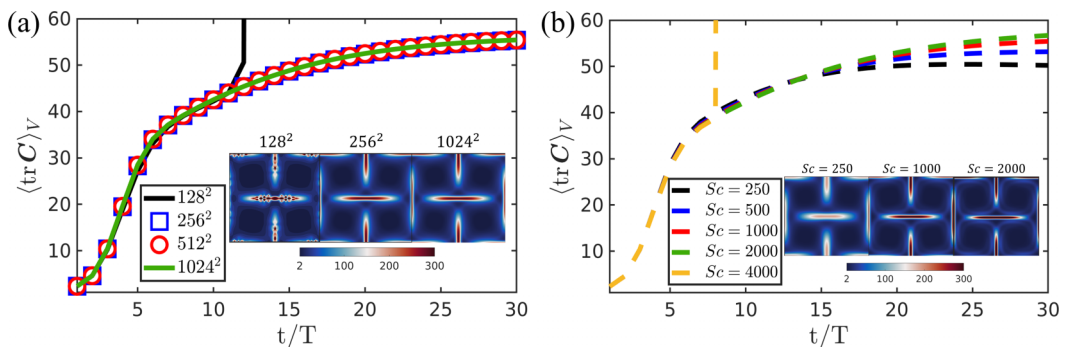
FIG. 17. Time series of the first component of the conformation tensor C_{xx} for FRM at the position $[\pi, \pi]$. Results are compared at Bi $= 0.2$ for (a) different grid resolutions, namely 128^2 (black), 256^2 (blue square), 512^2 (red circle), and 1024^2 (green). Analogous results are obtained with $(n \times N)^2 = 512^2$ in (b), however, at different levels of artificial diffusivity, namely Sc $= 250$ (black), Sc $= 500$ (blue), Sc $= 1000$ (red), Sc $= 2000$ (green), and Sc $= 4000$ (yellow). Note that the insets in (a) and (b) correspond to contour plots for tr(C) at different grid resolutions at $t = 12T$ and different Sc values at $t = 25T$, respectively.

unable to handle the steep polymer stress gradients that develop from the strong elongational effects, thus causing the simulation to rapidly diverge. For our hybrid LBM solver [48], we find that a grid resolution of $(n \times N)^2 = 256^2$ adequately resolves the qualitative and quantitative features of the problem, as similarly observed in previous numerical studies of inertialess viscoelastic instabilities using a periodic background forcing [49,53,55,68].

Additional numerical regularization terms in Eq. (2) are often required to preserve numerical stability [30], particularly in the case of simulating inertialess viscoelastic instabilities, which are renowned for producing steep polymer stress gradients that develop Hadamard instabilities [69]. A popular regularization technique involves adding an additional Laplace term, $\kappa \Delta C$ to the right-hand side of Eq. (2) to stabilize and regulate the buildup of steep polymer stress gradients at high elastic effects through a specified level of artificial diffusivity κ [30,49,50,53,55]. In Fig. 17(b) we compare different levels of κ by varying Sc, wherein large diffusivity levels (i.e., Sc $\leqslant 500$) smear the polymer field [refer to the inset in Fig. 17(b)], thereby suppressing strong polymer stretching behavior, as similarly observed in previous studies [50,53]. On the other hand, imposing small values of κ (i.e., Sc $= 4000$) is not sufficient in controlling the buildup of steep polymer stress gradients, thus resulting in numerical instability. Using a grid resolution of $(n \times N)^2 = 512^2$, we find that the results for Sc $= 1000$ and Sc $= 2000$ retrieve similar qualitative and quantitative flow behavior. Based on the results from Fig. 17(a) [i.e., using $(n \times N)^2 = 256^2$], we, therefore, select Sc $= 1000$ in our simulations to preserve numerical stability, which matches previous values used for κ in simulating inertialess viscoelastic instabilities [6,49,55].

---

[1] A. Groisman and V. Steinberg, Elastic turbulence in polymer solution flow, Nature (London) **405**, 53 (2000).

[2] A. Groisman and V. Steinberg, Elastic turbulence in curvilinear flows of polymer solutions, New J. Phys. **6**, 29 (2004).

[3] V. Steinberg, Elastic turbulence: An experimental view on inertialess random flow, Annu. Rev. Fluid Mech. **53**, 27 (2021).

[4] S. S. Datta, A. M. Ardekani, P. E. Arratia, A. N. Beris, I. Bischofberger, G. H. McKinley, J. G. Eggers, J. E. López-Aguilar, S. M. Fielding, A. Frishman, M. D. Graham, J. S. Guasto, S. J. Haward, A. Q. Shen, S. Hormozi, A. Morozov, R. J. Poole, V. Shankar, E. S. G. Shaqfeh, H. Stark *et al.*, Perspectives on viscoelastic flow instabilities and elastic turbulence, Phys. Rev. Fluids **7**, 080701 (2022).

[5] A. Groisman and V. Steinberg, Efficient mixing at low Reynolds numbers using polymer additives, Nature (London) **410**, 905 (2001).

[6] S. Berti, A. Bistagnino, G. Boffetta, A. Celani, and S. Musacchio, Two-dimensional elastic turbulence, Phys. Rev. E **77**, 055306(R) (2008).

[7] C. A. Browne and S. S. Datta, Elastic turbulence generates anomalous flow resistance in porous media, Sci. Adv. **7**, eabj2619 (2021).

[8] V. Steinberg, Scaling relations in elastic turbulence, Phys. Rev. Lett. **123**, 234501 (2019).

[9] C. A. Browne, A. Shih, and S. S. Datta, Bistability in the unstable flow of polymer solutions through pore constriction arrays, J. Fluid Mech. **890**, A2 (2020).

[10] M. Kumar, S. Aramideh, C. A. Browne, S. S. Datta, and A. M. Ardekani, Numerical investigation of multistability in the unstable flow of a polymer solution through porous media, Phys. Rev. Fluids **6**, 033304 (2021).

[11] V. Dzanic, C. S. From, A. Gupta, C. Xie, and E. Sauret, Geometry dependence of viscoelastic instabilities through porous media, Phys. Fluids **35**, 023105 (2023).

[12] V. Dzanic, C. S. From, Z. Wang, A. Gupta, C. Xie, and E. Sauret, Mobilization of trapped oil droplet in porous media through viscoelasticity, Phys. Fluids **35**, 093108 (2023).

[13] C. Xie and M. T. Balhoff, Lattice Boltzmann modeling of the apparent viscosity of thinning–elastic fluids in porous media, Transp. Porous Media **137**, 63 (2021).

[14] D. W. Carlson, K. Toda-Peters, A. Q. Shen, and S. J. Haward, Volumetric evolution of elastic turbulence in porous media, J. Fluid Mech. **950**, A36 (2022).

[15] A. Clarke, A. M. Howe, J. Mitchell, J. Staniland, L. Hawkes, and K. Leeper, Mechanism of anomalously increased oil displacement with aqueous viscoelastic polymer solutions, Soft Matter **11**, 3536 (2015).

[16] S. J. Haward, C. C. Hopkins, and A. Q. Shen, Stagnation points control chaotic fluctuations in viscoelastic porous media flow, Proc. Natl. Acad. Sci. USA **118**, e2111651118 (2021).

[17] D. M. Walkama, N. Waisbord, and J. S. Guasto, Disorder suppresses chaos in viscoelastic flows, Phys. Rev. Lett. **124**, 164501 (2020).

[18] T. M. Squires and S. R. Quake, Microfluidics: Fluid physics at the nanoliter scale, Rev. Mod. Phys. **77**, 977 (2005).

[19] P. C. Sousa, F. T. Pinho, and M. A. Alves, Purely-elastic flow instabilities and elastic turbulence in microfluidic cross-slot devices, Soft Matter **14**, 1344 (2018).

[20] H. Gan, Y. Lam, N.-T. Nguyen, K. Tam, and C. Yang, Efficient mixing of viscoelastic fluids in a microchannel at low Reynolds number, Microfluid. Nanofluid. **3**, 101 (2006).

[21] Y. Lam, H. Gan, N.-T. Nguyen, and H. Lie, Micromixer based on viscoelastic flow instability at low Reynolds number, Biomicrofluidics **3**, 014106 (2009).

[22] R. B. Bird, G. Dai, and B. J. Yarusso, The rheology and flow of viscoplastic materials, Rev. Chem. Eng. **1**, 1 (1983).

[23] N. J. Balmforth, I. A. Frigaard, and G. Ovarlez, Yielding to stress: Recent developments in viscoplastic fluid mechanics, Annu. Rev. Fluid Mech. **46**, 121 (2014).

[24] P. Saramito, A new constitutive equation for elastoviscoplastic fluid flows, J. Non-Newton. Fluid Mech. **145**, 1 (2007).

[25] S. Hormozi and I. A. Frigaard, Dispersion of solids in fracturing flows of yield stress fluids, J. Fluid Mech. **830**, 93 (2017).

[26] I. A. Frigaard, K. G. Paso, and P. R. de Souza Mendes, Bingham's model in the oil and gas industry, Rheol. Acta **56**, 259 (2017).

[27] A. Maleki and S. Hormozi, Submerged jet shearing of visco-plastic sludge, J. Non-Newton. Fluid Mech. **252**, 19 (2018).

[28] D. W. Bousfield, Rheological issues in the paper industry, Rheol. Rev. **6**, 47 (2008).

[29] M. Kumar, J. S. Guasto, and A. M. Ardekani, Transport of complex and active fluids in porous media, J. Rheol. **66**, 375 (2022).

[30] M. Alves, P. Oliveira, and F. Pinho, Numerical methods for viscoelastic fluid flows, Annu. Rev. Fluid Mech. **53**, 509 (2021).

[31] M. Abdelgawad, I. Cannon, and M. Rosti, Scaling and intermittency in turbulent flows of elastoviscoplastic fluids, Nat. Phys. **19**, 1059 (2023).

[32] M. E. Rosti, D. Izbassarov, O. Tammisola, S. Hormozi, and L. Brandt, Turbulent channel flow of an elastoviscoplastic fluid, J. Fluid Mech. **853**, 488 (2018).

[33] D. Fraggedakis, Y. Dimakopoulos, and J. Tsamopoulos, Yielding the yield-stress analysis: a study focused on the effects of elasticity on the settling of a single spherical particle in simple yield-stress fluids, Soft Matter **12**, 5378 (2016).

[34] S. Le Clainche, D. Izbassarov, M. Rosti, L. Brandt, and O. Tammisola, Coherent structures in the turbulent channel flow of an elastoviscoplastic fluid, J. Fluid Mech. **888**, A5 (2020).

[35] F. De Vita, M. Rosti, D. Izbassarov, L. Duffo, O. Tammisola, S. Hormozi, and L. Brandt, Elastoviscoplastic flows in porous media, J. Non-Newton. Fluid Mech. **258**, 10 (2018).

[36] S. Parvar, E. Chaparian, and O. Tammisola, General hydrodynamicfeatures of elastoviscoplastic fluid flows through randomised porous media, arXiv:2308.07435.

[37] D. Izbassarov and O. Tammisola, Dynamics of an elastoviscoplastic droplet in a newtonian medium under shear flow, Phys. Rev. Fluids **5**, 113301 (2020).

[38] I. Cheddadi, P. Saramito, B. Dollet, C. Raufaste, and F. Graner, Understanding and predicting viscous, elastic, plastic flows, Eur. Phys. J. E **34**, 1 (2011).

[39] B. Dollet and F. Graner, Two-dimensional flow of foam around a circular obstacle: Local measurements of elasticity, plasticity and flow, J. Fluid Mech. **585**, 181 (2007).

[40] A. M. V. Putz, T. I. Burghelea, I. A. Frigaard, and D. M. Martinez, Settling of an isolated spherical particle in a yield stress shear thinning fluid, Phys. Fluids **20**, 033102 (2008).

[41] E. Chaparian and O. Tammisola, An adaptive finite element method for elastoviscoplastic fluid flows, J. Non-Newton. Fluid Mech. **271**, 104148 (2019).

[42] E. Chaparian, D. Izbassarov, F. De Vita, L. Brandt, and O. Tammisola, Yield-stress fluids in porous media: a comparison of viscoplastic and elastoviscoplastic flows, Meccanica **55**, 331 (2019).

[43] S. Varchanis, S. J. Haward, C. C. Hopkins, A. Syrakos, A. Q. Shen, Y. Dimakopoulos, and J. Tsamopoulos, Transition between solid and liquid state of yield-stress fluids under purely extensional deformations, Proc. Natl. Acad. Sci. USA **117**, 12611 (2020).

[44] J. G. Oldroyd, On the formulation of rheological equations of state, Proc. R. Soc. Lond. A **200**, 523 (1950).

[45] D. F. James, Boger fluids, Annu. Rev. Fluid Mech. **41**, 129 (2009).

[46] P. Saramito, A new elastoviscoplastic model based on the herschel–bulkley viscoplastic model, J. Non-Newton. Fluid Mech. **158**, 154 (2009).

[47] C. J. Dimitriou and G. H. McKinley, A canonical framework for modeling elasto-viscoplasticity in complex fluids, J. Non-Newton. Fluid Mech. **265**, 116 (2019).

[48] V. Dzanic, C. S. From, and E. Sauret, A hybrid lattice Boltzmann model for simulating viscoelastic instabilities, Comput. Fluids **235**, 105280 (2022).

[49] V. Dzanic, C. From, and E. Sauret, The effect of periodicity in the elastic turbulence regime, J. Fluid Mech. **937**, A31 (2022).

[50] V. Dzanic, C. S. From, and E. Sauret, Conserving elastic turbulence numerically using artificial diffusivity, Phys. Rev. E **106**, L013101 (2022).

[51] V. Dzanic, C. From, and E. Sauret, Assessment of polymer feedback coupling approaches in simulation of viscoelastic fluids using the lattice Boltzmann method, Comput. Fluids **246**, 105629 (2022).

[52] A. Kurganov and E. Tadmor, New high-resolution central schemes for nonlinear conservation laws and convection–diffusion equations, J. Comput. Phys. **160**, 241 (2000).

[53] A. Gupta and D. Vincenzi, Effect of polymer-stress diffusion in the numerical simulation of elastic turbulence, J. Fluid Mech. **870**, 405 (2019).

[54] B. Thomases and M. Shelley, Emergence of singular structures in Oldroyd-B fluids, Phys. Fluids **19**, 103103 (2007).

[55] B. Thomases and M. Shelley, Transition to mixing and oscillations in a Stokesian viscoelastic flow, Phys. Rev. Lett. **103**, 094501 (2009).

[56] B. Thomases, An analysis of the effect of stress diffusion on the dynamics of creeping viscoelastic flow, J. Non-Newton. Fluid Mech. **166**, 1221 (2011).

[57] T. Vaithianathan and L. R. Collins, Numerical approach to simulating turbulent flow of a viscoelastic polymer solution, J. Comput. Phys. **187**, 1 (2003).

[58] B. Thomases, M. Shelley, and J.-L. Thiffeault, A Stokesian viscoelastic flow: Transition to oscillations and mixing, Physica D **240**, 1602 (2011).

[59] H. Garg, E. Calzavarini, G. Mompean, and S. Berti, Particle-laden two-dimensional elastic turbulence, Eur. Phys. J. E **41**, 115 (2018).

[60] E. L. C. V. M. Plan, A. Gupta, D. Vincenzi, and J. D. Gibbon, Lyapunov dimension of elastic turbulence, J. Fluid Mech. **822**, R4 (2017).

[61] O. Cardoso, D. Marteau, and P. Tabeling, Quantitative experimental study of the free decay of quasi-two-dimensional turbulence, Phys. Rev. E **49**, 454 (1994).

[62] D. M. Rothstein, E. Henry, and J. P. Gollub, Persistent patterns in transient chaotic fluid mixing, Nature (London) **401**, 770 (1999).

[63] B. Liu, M. Shelley, and J. Zhang, Oscillations of a layer of viscoelastic fluid under steady forcing, J. Non-Newton. Fluid Mech. **175-176**, 38 (2012).

[64] K. Gotoh and M. Yamada, Instability of a cellular flow, J. Phys. Soc. Jpn. **53**, 3395 (1984).

[65] P. E. Arratia, C. C. Thomas, J. Diorio, and J. P. Gollub, Elastic instabilities of polymer solutions in cross-channel flow, Phys. Rev. Lett. **96**, 144502 (2006).

[66] See Supplemental Material at http://link.aps.org/supplemental/10.1103/PhysRevFluids.9.063301 for supplementary movies of the polymer field at different Bingham numbers.

[67] D. Izbassarov, M. E. Rosti, L. Brandt, and O. Tammisola, Effect of finite Weissenberg number on turbulent channel flows of an elastoviscoplastic fluid, J. Fluid Mech. **927**, A45 (2021).

[68] S. R. Yerasi, J. R. Picardo, A. Gupta, and D. Vincenzi, Preserving large-scale features in simulations of elastic turbulence, arXiv:2312.09165.

[69] R. Sureshkumar and A. N. Beris, Effect of artificial stress diffusivity on the stability of numerical calculations and the flow dynamics of time-dependent viscoelastic flows, J. Non-Newton. Fluid Mech. **60**, 53 (1995).